



# A 9.2-GHz clock transition in a Lu(II) molecular spin qubit arising from a 3,467-MHz hyperfine interaction

Krishnendu Kundu<sup>1</sup>, Jessica R. K. White<sup>2</sup>, Samuel A. Moehring<sup>2</sup>, Jason M. Yu<sup>2</sup>, Joseph W. Ziller<sup>2</sup>, Filipp Furche<sup>2</sup>✉, William J. Evans<sup>2</sup>✉ and Stephen Hill<sup>1,3</sup>✉

**Spins in molecules are particularly attractive targets for next-generation quantum technologies, enabling chemically programmable qubits and potential for scale-up via self-assembly. Here we report the observation of one of the largest hyperfine interactions for a molecular system,  $A_{\text{iso}} = 3,467 \pm 50$  MHz, as well as a very large associated clock transition. This is achieved through chemical control of the degree of *s*-orbital mixing into the spin-bearing *d* orbital associated with a series of spin- $\frac{1}{2}$  La(II) and Lu(II) complexes. Increased *s*-orbital character reduces spin-orbit coupling and enhances the electron-nuclear Fermi contact interaction. Both outcomes are advantageous for quantum applications. The former reduces spin-lattice relaxation, and the latter maximizes the hyperfine interaction, which, in turn, generates a 9-GHz clock transition, leading to an increase in phase memory time from  $1.0 \pm 0.4$  to  $12 \pm 1$   $\mu\text{s}$  for one of the Lu(II) complexes. These findings suggest strategies for the development of molecular quantum technologies, akin to trapped ion systems.**

The field of quantum information science is witnessing remarkable progress, with prototype devices reaching the point of practical quantum advantage<sup>1</sup>. The fundamental building block of a quantum computer is the physical quantum bit, or qubit, which can be any two-state quantum system. Many candidates are currently under investigation, including superconducting circuits<sup>2</sup>, trapped ions<sup>3</sup>, photons<sup>4</sup>, topological states in condensed matter<sup>5</sup>, as well as electron and nuclear spins in solids<sup>6,7</sup> or on surfaces<sup>8,9</sup>. However, continued scale-up to the point where fault-tolerant quantum logic is possible with vast numbers of qubits remains challenging. For this reason, research focusing on next-generation quantum technologies is very active<sup>10</sup>.

The  $S = \frac{1}{2}$  spin associated with an unpaired electron represents one of the simplest examples of a two-state quantum system that is easily manipulated using decades-old and well-understood magnetic resonance techniques<sup>11</sup>. Nature provides a rich, albeit finite, variety of quantum states in atoms and ions that may be trapped and organized into arrays with controllable interactions<sup>3</sup>. By comparison, coordination chemistry affords almost limitless tunability of the quantum states associated with unpaired electron spins in molecules, while also offering routes to large-scale assembly via supramolecular approaches<sup>12</sup>. However, this flexibility comes at a cost in terms of coherence due to the inherent coupling to magnetic and vibrational modes associated with the environment. In spite of this, excellent phase memory times ( $T_m$ ) have been demonstrated for isolated molecular spin qubits<sup>13</sup>. Further protection from magnetic noise has been achieved via the engineering of so-called clock transitions<sup>10,14–17</sup>—avoided level crossings associated with the Zeeman splitting of qubit states such that the transition frequency,  $f$ , becomes insensitive to the local magnetic induction,  $B_0$ , that is,  $df/dB_0 \rightarrow 0$  at the splitting minimum,  $\Delta_{\text{CT}}$  (Fig. 1a). In the first molecular example, an avoided crossing was generated via off-diagonal crystal-field terms in the Hamiltonian matrix of a Ho(III) ion

([Xe]4f<sup>0</sup> electronic configuration) encapsulated within a polyoxometalate cage<sup>18</sup>, resulting in a substantial  $T_m$  enhancement for a crystal rich in fluctuating electron and nuclear spins<sup>14</sup>. Although providing important insights, the Ho(III) example also highlighted limitations of crystal-field engineered clock transitions. In particular, achieving clock transition frequencies in the gigahertz range relies on spin-orbit coupling (SOC), which also promotes spin-lattice ( $T_1$ ) relaxation<sup>14</sup>. For these reasons, attention has shifted to alternative mechanisms for generating clock transitions, including electron-nuclear hyperfine interactions<sup>15</sup> and microwave dressing<sup>19</sup>.

In this Article we demonstrate the viability of coordination chemistry for engineering hyperfine clock transitions in magnetic molecules with tunable operating frequencies up to  $\sim 10$  GHz. The discovery that 4f<sup>n</sup> Ln(III) complexes of Ln = La, Ce, Pr, Gd, Tb, Ho, Er and Lu in the appropriate ligand environments can be reduced to 4f<sup>n</sup>5d<sup>1</sup> Ln(II) complexes<sup>20–24</sup> rather than the traditional 4f<sup>n+1</sup> Ln(II) previously found for Eu, Yb, Sm and Tm<sup>22,25</sup> has provided an alternative type of rare-earth electron configuration for development in quantum information science (QIS). The La(II) and Lu(II) congeners feature closed shell core configurations ([Xe] and [Xe]4f<sup>14</sup>, respectively) and a single  $S = \frac{1}{2}$  unpaired electron residing in an orbital with mixed 5d/6s character. By varying the ligands in these Ln(II) complexes<sup>24</sup>, synthetic control over the degree of *s*-orbital character that dominates the Fermi contact interaction with the associated nucleus provides a means of tuning the hyperfine interaction strength. As an added bonus, the dominant isotopes of both metals have large  $I = 7/2$  nuclear moments (99.9% and 97.4% natural abundance for <sup>139</sup>La and <sup>175</sup>Lu, respectively), which further enhances the corresponding clock transition frequency, thus reducing the second-order sensitivity to magnetic noise,  $d^2f/dB_0^2 \propto \Delta_{\text{CT}}^{-1}$  (refs. 14,26). Moreover, increased *s*-orbital character minimizes SOC, resulting in reduced spin-lattice relaxation relative to most Ln species with spin-orbital moments

<sup>1</sup>National High Magnetic Field Laboratory, Florida State University, Tallahassee, FL, USA. <sup>2</sup>Department of Chemistry, University of California, Irvine, CA, USA. <sup>3</sup>Department of Physics, Florida State University, Tallahassee, FL, USA. ✉e-mail: [filipp.furche@uci.edu](mailto:filipp.furche@uci.edu); [wevans@uci.edu](mailto:wevans@uci.edu); [shill@magnet.fsu.edu](mailto:shill@magnet.fsu.edu)

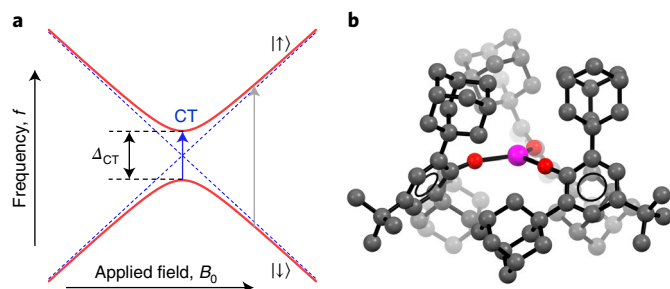


**Fig. 1 | Clock transition and  $[\text{Lu}(\text{OAr}^*)_3]^-$  structure.** **a**, Schematic  $f$  versus  $B_0$  energy diagram for a two-state quantum system (spin-up,  $|\uparrow\rangle$ , spin-down,  $|\downarrow\rangle$ ) illustrating the concept of a clock transition, where a term in the spin Hamiltonian that does not commute with the linear Zeeman interaction (blue dashed lines) gives rise to an avoided level crossing (red curves). The clock transition (blue arrow) occurs at the gap minimum,  $\Delta_{\text{CT}}$ , whereas normal EPR transitions occur away from this region (grey arrow). **b**, Ball-and-stick representation of the  $[\text{Lu}(\text{OAr}^*)_3]^-$  anion of complex **4**. Lu, pink; O, red; C, light/dark grey. H atoms are omitted for clarity.

$J > \frac{1}{2}$  (ref. 27). These factors give rise to a molecular qubit platform similar to the  $^{171}\text{Yb}^+$  ion (formally  $[\text{Xe}]4f^{14}6s^1$ ,  $I = \frac{1}{2}$ ) that is ubiquitous in the ion trap QIS community<sup>3</sup>, but with the added benefit of chemical tunability.

## Results and discussion

**The La(II) and Lu(II) compounds.** Potassium reduction of the tris(cyclopentadienyl) Lu(III) complex,  $\text{Cp}'_3\text{Lu}$  ( $\text{Cp}' = \text{C}_5\text{H}_4\text{SiMe}_3$ ) in the presence of 2.2.2-cryptand (crypt) generates a product,  $[\text{K}(\text{crypt})][\text{Cp}'_3\text{Lu}]$  (**1**), containing a Lu(II) ion whose electron configuration is formally  $4f^{14}5d^1$  based on density functional calculations<sup>21</sup>. The low-field (X-band:  $f = 9.7$  GHz and  $B_0 < 1$  T) electron paramagnetic resonance (EPR) spectrum of complex **1** displays an eight-line pattern due to the lone unpaired electron ( $S = \frac{1}{2}$ ) and its hyperfine coupling with the  $I = \frac{7}{2}$   $^{175}\text{Lu}$  isotope<sup>21</sup>. The average hyperfine coupling constant,  $A_{\text{iso}} = 428.5$  G, was the largest observed for any Lu complex, suggesting significant  $s$ -orbital character in **1**<sup>28,29</sup>. Meanwhile, similar reduction of the tris(amide)  $\text{Lu}(\text{NR}_2)_3$  ( $\text{R} = \text{SiMe}_3$ ) and tris(aryloxy)  $\text{Lu}(\text{OAr}^*)_3$  ( $\text{OAr}^* = 2,6\text{-Ad}_2\text{-}4\text{-Bu-C}_6\text{H}_3\text{O}$ , where Ad is adamantyl) also gives rise to formally  $4f^{14}5d^1$  Lu(II) complexes. However, the X-band EPR spectra do not display the expected eight-line patterns. Because the hyperfine constants of the analogous yttrium tris(amide)  $[\text{K}(\text{crypt})][\text{Y}(\text{NR}_2)_3]$  and tris(aryloxy)  $[\text{K}(\text{crypt})][\text{Y}(\text{OAr}^*)_3]$  ( $A_{\text{iso}} = 110$  G and 156.5 G, respectively)<sup>23,24</sup> are much larger than that of tris(cyclopentadienyl)  $[\text{K}(\text{crypt})][\text{YCp}'_3]$  ( $A_{\text{iso}} = 36.6$  G), this suggests that the hyperfine constants of the corresponding Lu(II) complexes are much larger than the 428.5 G value of **1**. Accordingly, we conducted high-field (W band:  $f = 94$  GHz and  $B_0 = 3\text{--}4$  T) EPR investigations of the reduced Ln(II) products  $[\text{La}(\text{OAr}^*)_3]^-$  (**2**),  $[\text{Lu}(\text{NR}_2)_3]^-$  (**3**) and  $[\text{Lu}(\text{OAr}^*)_3]^-$  (**4**). Complex **4** (Fig. 1b) is found to have a huge hyperfine interaction,  $A_{\text{iso}} = 3,467 \pm 50$  MHz, giving rise to a giant clock transition and the enhanced coherence central to this investigation. To our knowledge, the only larger molecular hyperfine interaction in the literature is the 3,799-MHz value reported for a Bi(II) radical<sup>30,31</sup>, although theoretical predictions of large hyperfine interactions have been suggested for Tb(II)<sup>32</sup>.

**EPR studies.** Analysis of the EPR spectra of **2–4** is carried out according to the effective spin Hamiltonian of equation (1) describing a lone  $S = \frac{1}{2}$  electron coupled to an  $I = \frac{7}{2}$  nuclear spin (see Methods for further details)<sup>33</sup>.

$$\hat{H} = \mu_B \mathbf{B}_0 \cdot \overleftrightarrow{g}_e \cdot \hat{S} - \mu_N g_N \mathbf{B}_0 \cdot \hat{I} + \hat{S} \cdot \overleftrightarrow{A} \cdot \hat{I} + \hat{I} \cdot \overleftrightarrow{Q} \cdot \hat{I} \quad (1)$$

where the first two terms respectively denote the electron and nuclear Zeeman interactions ( $\overleftrightarrow{g}_e$  is the electron  $g$ -tensor) and the third term represents the electron–nuclear hyperfine interaction ( $\overleftrightarrow{A}$  is the hyperfine coupling tensor). Meanwhile, for **3** and **4**, our analysis requires a nuclear quadrupole interaction (NQI) specified by the matrix  $\overleftrightarrow{Q}$  (ref. 34). Precise constraint of the anisotropic  $\overleftrightarrow{g}_e$ ,  $\overleftrightarrow{A}$  and  $\overleftrightarrow{Q}$  tensors is aided by performing measurements in a high-field regime dominated by the electron Zeeman interaction. In this limit, the electron and nuclear spin projection quantum numbers,  $m_s$  and  $m_I$ , are exact. As seen in Fig. 2a,b, this leads to a linear Zeeman splitting of the  $m_s = \pm \frac{1}{2}$  states, each of which is further split into eight sub-levels due to the hyperfine interaction with the  $I = \frac{7}{2}$  nuclear spin (we neglect minority isotopes).

Pulsed electron-spin echo (ESE) measurements were performed at 94 GHz (ref. 35) on frozen solutions containing a uniform distribution of molecular orientations (10 mM in tetrahydrofuran;

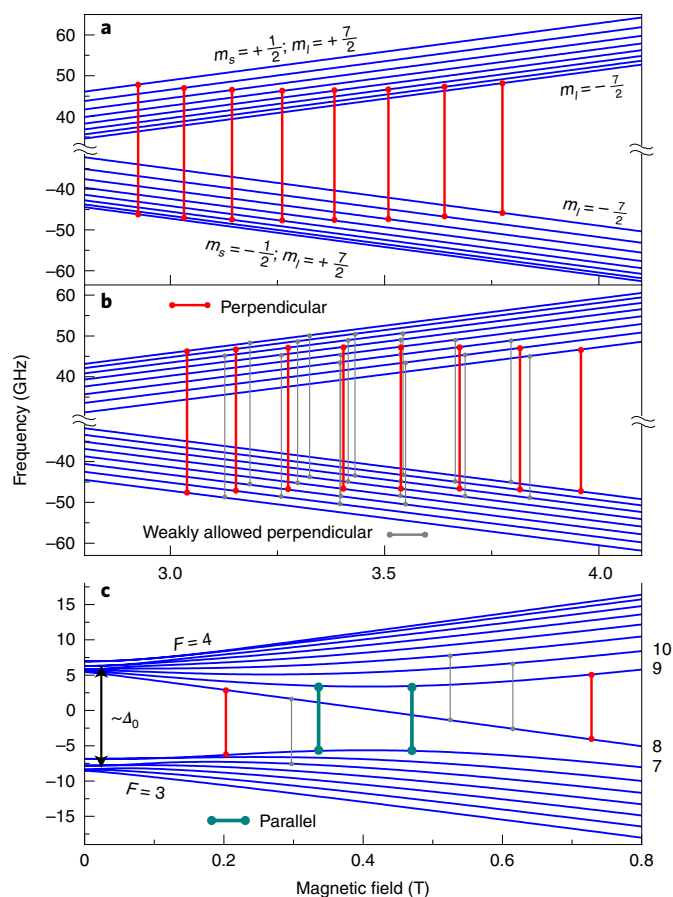


**Fig. 2 |  $[\text{Lu}(\text{OAr}^*)_3]^-$  Zeeman diagrams.** **a–c**, Simulated energy diagrams for the  $\mathbf{B}_0||z$  (**a**) and  $\mathbf{B}_0||xy$  (**b,c**) orientations of the applied magnetic field, corresponding to regions of interest in the W-band (**a,b**) and X-band (**c**) EPR spectra of complex **4**. The simulations were generated according to equation (1) using the parameters listed in Table 1. Some of the levels in **a** have been labelled according to the associated  $m_s$  and  $m_I$  spin projections appropriate to the high-field limit, and a few of the levels are numbered on the right side of **c** to aid discussion of the X-band spectra. Allowed and weakly allowed transitions are indicated by vertical lines (corresponding to 94 GHz in **a,b** and 9.2 GHz in **c**) both for conventional perpendicular ( $\pi$ ) and parallel ( $\sigma$ ) mode excitation. The zero-field gap,  $\Delta_0$ , between electron–nuclear hyperfine multiplets is indicated in **c**.

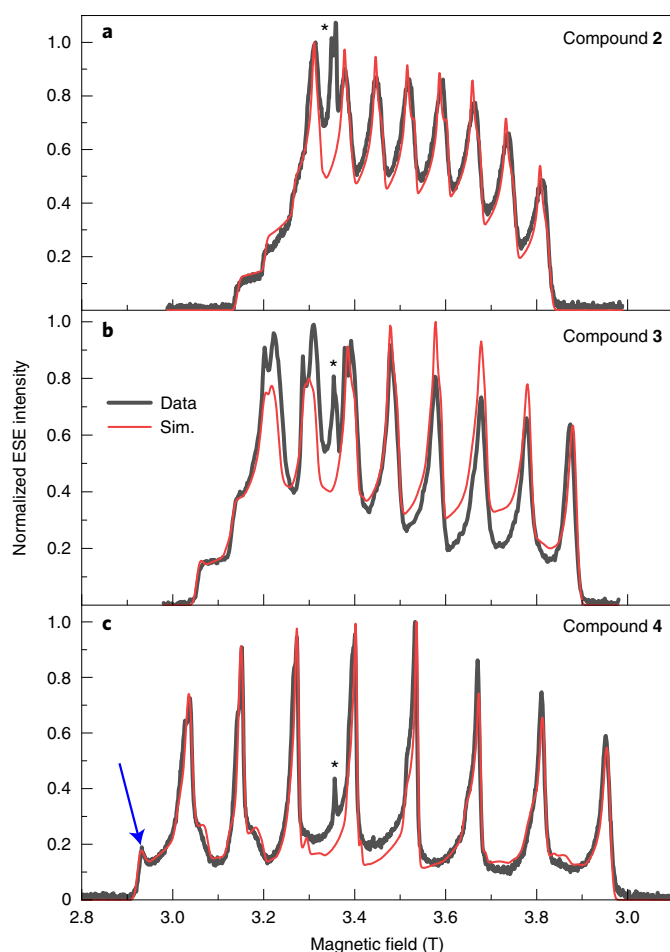


**Fig. 3 | ESE-detected W-band spectra. a–c**, Experimental ESE spectra (black) and simulations (red) recorded at the W-band frequency of 94.0 GHz and  $T=5.0$  K for frozen solution samples of compounds **2** (a), **3** (b) and **4** (c). Asterisks denote a  $g=2.00$  electron in the solution, and the blue arrow denotes a region of the spectrum of **4** that is highly sensitive to the NQI (Extended Data Fig. 1b).

Methods). Experimental spectra are displayed together with the best simulations for compounds 2–4 in Fig. 3. We focus on compound 4 in the following discussion. The high-field selection rule requires  $\Delta m_s = \pm 1$  and  $\Delta m_l = 0$ , resulting in eight allowed transitions for each molecular orientation, as denoted by vertical red lines in Fig. 2a ( $\mathbf{B}_0 \parallel z$ ) and 2b ( $\mathbf{B}_0 \parallel x$ ). The axial nature of the  $\vec{g}_e$ -tensor for **4** ( $g_{zz} > g_{xx} = g_{yy}$ ) is such that molecules with  $\mathbf{B}_0 \parallel xy$  provide the strongest weight, resulting in the eight sharp peaks (one for each  $m_l$  value) with sharp intensity drop-off at their high-field edges. The remaining molecules in the orientational distribution (with  $g > g_{xx,yy}$ ) result in the slower decay in intensity on the low-field sides of each peak (Extended Data Fig. 1a). The average peak spacing,  $\Delta B_0$  (~131 mT for **4**), is given approximately by the value of  $A_{xx}$ , which can be seen to increase from compound **2** to **4** (Table 1).

As seen in Fig. 2, the  $g$ -anisotropy (which dictates the span from  $\mathbf{B}_0 \parallel z$  to  $\mathbf{B}_0 \parallel xy$  for each transition) results in complete overlap of adjacent hyperfine peaks. The uneven peak spacing is due in part to the fact that the true high-field limit has not quite been reached. However, optimal reproduction of the peak spacings and linewidths (for example, narrower peaks at the centre of the spectrum) requires inclusion of a sizeable NQI, which causes an uneven spacing of  $m_l$  levels and the pronounced bunching at the lowest energies in Fig. 2a. Importantly, this accounts for the sharp upturn in intensity seen at

**Table 1 | Spin Hamiltonian parameters**

	2	3	4
<b>Experiment</b>			
$A_{xx}$ (MHz) <sup>a</sup>	$1,870 \pm 25$	$2,480 \pm 50$	$3,500 \pm 50$
$A_{yy}$ (MHz) <sup>a</sup>	$1,870 \pm 25$	$2,550 \pm 50$	$3,500 \pm 50$
$A_{zz}$ (MHz) <sup>a</sup>	$1,780 \pm 25$	$2,300 \pm 50$	$3,400 \pm 50$
$A_{iso}$ (MHz) <sup>a</sup>	$1,840 \pm 25$	$2,443 \pm 50$	$3,467 \pm 50$
$Q_{zz}$ (MHz)	0	$60 \pm 20$	$100 \pm 20$
$g_{xx}$	$1.876 \pm 0.002$	$1.882 \pm 0.002$	$1.915 \pm 0.002$
$g_{yy}$	$1.886 \pm 0.002$	$1.898 \pm 0.002$	$1.915 \pm 0.002$
$g_{zz}$	$2.000 \pm 0.002$	$2.000 \pm 0.002$	$2.000 \pm 0.002$
$\Delta_A$ (MHz) <sup>b</sup>	100	100	100
$lw_{pp}$ (mT) <sup>b</sup>	8	5	5
<b>Theory</b>			
$A_{iso}^{point}$ (MHz)	9,040	19,530	27,360
$A_{iso}^{finite}$ (MHz)	8,274	17,040	23,950
$Q_{zz}$ (MHz)	0.436	11.2	15.9

<sup>a</sup> Uncertainties refer to the mean values of the associated distributions. <sup>b</sup> A-strain ( $\Delta_A$ ) and peak-to-peak linewidths ( $lw_{pp}$ ) used for simulations with no associated uncertainties; values correspond to the full-width at half maximum (FWHM) of the distribution ( $=2.35\sigma$ , where  $\sigma$  is s.d.). Values are obtained from the best simulations of the experimental data (errors denote estimated uncertainties) and from theory (no associated uncertainties) for the three compounds (2–4) investigated in this work.

the very low-field end of the spectrum (Fig. 3c and Extended Data Fig. 1b), which cannot otherwise be reproduced in the simulations. The NQI breaks zero-field rotational invariance, resulting in relaxation of the  $\Delta m_l = 0$  selection rule so that additional transitions become weakly allowed as  $\mathbf{B}_0$  rotates away from the molecular  $z$  axis (Fig. 2b). This accounts for shoulders on the high-field edges of some of the peaks in Fig. 3c, as well as a prominent X-band peak (see below). The parameters employed for the best simulations, which also consider strains (distributions), are given in Table 1 for 2–4.

We next consider the intermediate field regime where the hyperfine clock transitions are observed. At zero field, the hyperfine interaction is dominant, resulting in a pair of electron–nuclear multiplets with total angular momentum  $F = I \pm S = 7/2 \pm 1/2 = 4$  and 3. The ordering of these states depends on the sign of  $A_{iso}$  ( $=1/3 \text{Tr}(\vec{A})$ ), which we know to be positive from theoretical considerations, hence  $F=3$  lies lowest in energy. In the absence of an NQI, the gap separating the multiplets is given by  $\Delta_0 = \frac{7}{2} A_{iso}$ . One sees here that the large nuclear moment amplifies this gap and, consequently, increases the corresponding hyperfine clock transition frequencies. Inclusion of the NQI results in weak zero-field splitting of the spin projection states ( $m_F = 0, \pm 1, \dots, \pm F$ ) within each  $F$  multiplet (Fig. 2c), as well as a slight enhancement of  $\Delta_0$  ( $=13.9$  GHz between centroids of the  $F=3$  and 4 multiplets for **4**). Application of a magnetic field splits the  $m_F$  states. In the field range where the hyperfine and electron Zeeman energies are comparable, off-diagonal elements of the Hamiltonian give rise to a repulsion between states belonging to different  $F$  multiplets. This accounts for the evolution from a pair of coupled electron–nuclear states at low fields, with multiplicities  $2F+1=9$  and 7, into a pair of decoupled  $m_s$  states at high fields, each with multiplicity  $(2I+1)=8$ . Crucially, the resultant avoided level crossings give rise to hyperfine clock transitions. Neither the  $[F, m_F]$  nor  $[m_s, m_l]$  labels are appropriate in this regime, so the relevant states are numbered in Fig. 2c. Of most interest is the  $7 \rightarrow 9$  transition for **4**, which gives rise to hyperfine clock transitions spanning from 8.92 to 9.25 GHz for the orientational distribution in the solution sample (Fig. 4a). This frequency is close to the

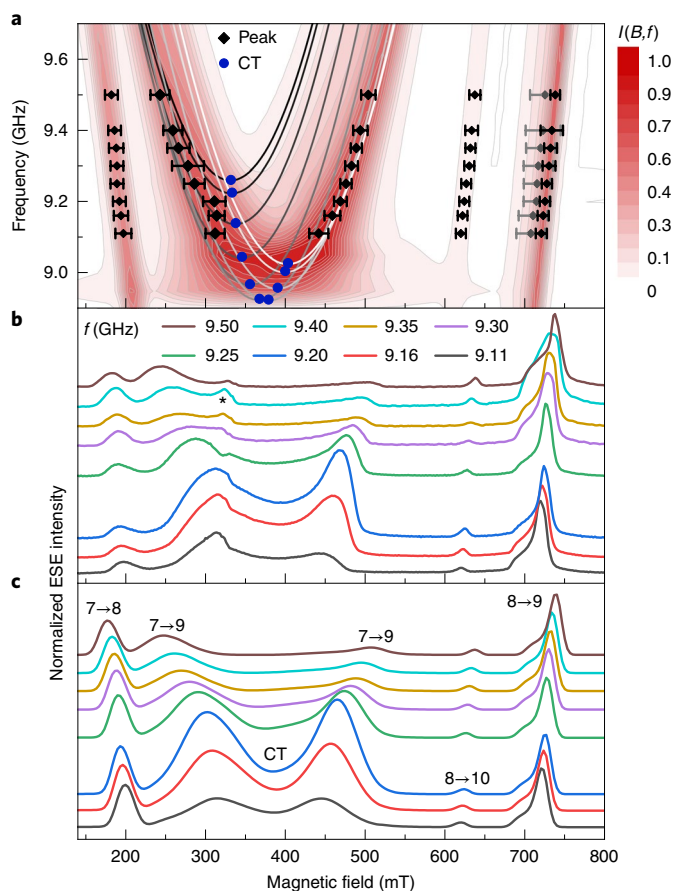


**Fig. 4** |  $[\text{Lu}(\text{OAr}^+)_3]^-$  ESE-detected X-band spectra. **a, b**, Two-dimensional plot of peak positions (**a**, grey and black data points) deduced from the ESE spectra in **b**, recorded as a function of frequency (see legend) at  $T = 5.0$  K for a frozen solution of compound **4**. Error bars denote  $\pm$ s.d. deduced from Gaussian fits to individual peaks in **b**, and the asterisk denotes a  $g = 2.00$  electron signal. **c**, Corresponding perpendicular-mode simulations generated according to equation (1), with a frequency-dependent admixture of the parallel-mode spectrum (Methods). The main resonances are labelled according to the energy level numbering scheme in Fig. 2c. The coloured intensity map,  $I(B, f)$ , in **a** was generated according to a similar procedure to the simulations in **c**. Solid curves correspond to the transition frequencies for different molecular orientations ( $\mathbf{B}_0 \parallel z$  (dark) to  $\mathbf{B}_0 \parallel xy$  (white) in  $10^\circ$  steps).

12.6-GHz hyperfine clock transition found for the  $^{171}\text{Yb}^+$  ion qubit<sup>3</sup> that is also used as a frequency standard<sup>36</sup> and, to the best of our knowledge, exceeds all known solid-state and molecular hyperfine clock transition frequencies, for example,  $^{209}\text{Bi}$  donors in  $\text{Si}^{26}$ .

The  $7 \rightarrow 9$  transition is strongest for parallel-mode excitation ( $\mathbf{B}_1 \parallel \mathbf{B}_0$ , where  $\mathbf{B}_1$  is the magnetic component of the microwave field). However, the NQI also results in perpendicular-mode ( $\mathbf{B}_1 \perp \mathbf{B}_0$ ) intensity (Extended Data Fig. 2). Figure 4b displays ESE-detected spectra for **4** recorded at frequencies from 9.11 to 9.50 GHz, with corresponding simulations in Fig. 4c. The various peaks are labelled accordingly, and their frequency versus field behaviour compared to simulations in Fig. 4a. The dominant resonances fall into two categories: the standard perpendicular-mode  $\pi$  transitions, which conserve  $m_l$  in the high-field limit, and parallel-mode  $\sigma$  transitions that may involve simultaneous electron and nuclear spin flips, for example, the zero-quantum transition,  $\Delta m_s = +1$ ,  $\Delta m_l = -1$ . The X-band spectra are dominated by the  $7 \rightarrow 8$  and  $8 \rightarrow 9$   $\pi$  transitions at the extremities and the  $7 \rightarrow 9$  transitions at the centre. Satisfactory simulations

of both the X- and W-band spectra of **4** are only obtained when including the NQI, for example, the  $8 \rightarrow 10$  transition is completely absent otherwise (Extended Data Fig. 2). Meanwhile, the  $7 \rightarrow 9$  transitions are significantly stronger than expected based on the assumed  $\mathbf{B}_1 \perp \mathbf{B}_0$  polarization in the employed X-band resonator, particularly below 9.3 GHz. This is due to a known contamination of perpendicular-mode spectra with a parallel-mode component<sup>14</sup>. Therefore, the simulations in Fig. 4c were generated by adding a frequency-dependent parallel-mode component to the perpendicular-mode spectra (Methods). This procedure does not influence the resonance positions, which agree well with simulations.

An important difference between the present study and the work in ref. <sup>14</sup> is the highly anisotropic nature of the Ho(III) ion, which required measurements on aligned dilute crystals. In the present case, a suitable diamagnetic host for Lu(II) doping has not yet been identified. However, the weak anisotropies in  $\langle \hat{g} \rangle$  and  $\langle \hat{A} \rangle$  found for **4** result in very small spreads in the solution ensemble hyperfine clock transition fields and frequencies (Fig. 4a), which span from 300 to 410 mT and 8.92 to 9.25 GHz. We therefore performed  $T_m$  measurements on a frozen solution across this region, the results of which are summarized in Fig. 5a. A broad peak is observed that is dominated by the  $7 \rightarrow 9$  ESE intensity. The  $T_m$  divergence is less pronounced in comparison to ref. <sup>14</sup> because of the distribution of  $T_m$  values at each field or frequency. At short delay times ( $2\tau < 5 \mu\text{s}$ ), a factor of  $\sim 4$  enhancement in  $T_m$  is observed relative to the normal (linear in  $B_0$ )  $\pi$  transitions. The A-strain inferred from simulations (Table 1) results in vertical broadening of the hyperfine clock transition frequencies (FWHM  $\approx 250$  MHz) so that molecules with  $\mathbf{B}_0 \parallel xy$  that dominate the orientational distribution can influence the measured  $T_m$  at frequencies as high as 9.20 GHz. This is why the maximum enhancement occurs at  $\sim 400$  mT. Meanwhile, at frequencies above 9.20 GHz, the  $T_m$  value shortens and the peak shifts to lower fields because the  $\mathbf{B}_0 \parallel xy$  hyperfine clock transitions are no longer accessible.

It is possible to sharpen the  $T_m$  divergence by recording ESE spectra at longer delay times (Fig. 5b), in effect narrowing in on (selecting) only those molecules in the distribution that have not yet dephased. At short times, the ESE intensity is dominated by the transition probability and orientational density of states (DOS), which is why the  $7 \rightarrow 9$  peaks occur away from the hyperfine clock transition fields. At long delay times, the ESE intensity is dominated by  $T_m$  and only molecules at the hyperfine clock transitions can be refocused. This explains why intensity is limited to the 300–410 mT range with a profile that reflects the orientational DOS-weighted distribution of hyperfine clock transition fields; that is, the peak occurs for molecules with  $\mathbf{B}_0 \parallel xy$  (Supplementary Section 3). A plot of the 410-mT ESE intensity versus delay time (Fig. 5a, inset) reveals a stretched exponential behaviour with an initial  $T_m = 3.2 \pm 0.1 \mu\text{s}$ , extending to  $12 \pm 1 \mu\text{s}$  at the longest delays, an order of magnitude enhancement relative to the  $\pi$  transitions ( $T_m^{\pi} = 1.0 \pm 0.4 \mu\text{s}$ ). Meanwhile, much longer  $T_1$  times ( $\sim 1.5$  ms) are deduced that are insensitive to the clock transition physics (Extended Data Fig. 3), suggesting an ultimate  $T_m$  limit far exceeding that found for crystal-field engineered clock transitions<sup>14</sup>.

Several trends are immediately apparent from the simulation parameters in Table 1. First and foremost is the ordering of the hyperfine interaction strength,  $A_{\text{iso}}(\mathbf{2}) < A_{\text{iso}}(\mathbf{3}) < A_{\text{iso}}(\mathbf{4})$ . This indicates increasing  $s$ -orbital character from **2** to **4**, a trend that is reversed for the  $\langle \hat{g}_c \rangle$ -tensor anisotropy, as expected because a more spherical  $s$ -orbital character will result in weaker SOC anisotropy. The other very obvious finding is the fact that an NQI is not detected for **2**, in contrast to **3** and **4**. This is consistent with the much larger quadrupole moment for  $^{175}\text{Lu}$  [3.49(2) barn] compared to  $^{139}\text{La}$  [0.200(2) barn]<sup>37</sup>.

**Electronic structure calculations.** To analyse the electronic structure responsible for the observed hyperfine and nuclear quadrupole interactions, scalar relativistic exact two-component (x2c) density

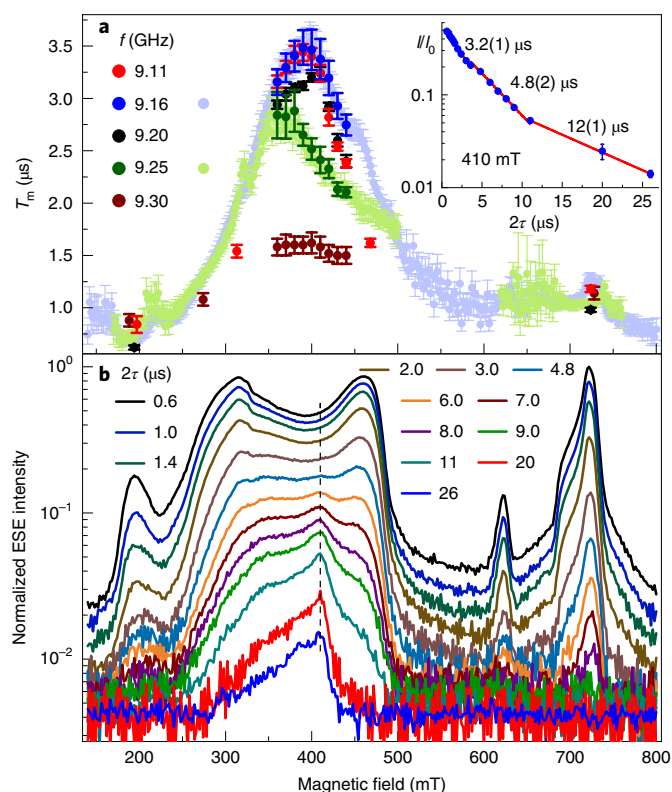


**Fig. 5** |  $[\text{Lu}(\text{OAr}^*)_3]$ - relaxation measurements. **a**, Phase memory time as a function of applied field and frequency at 5 K. Error bars denote the standard error in  $T_m$ . **b**, Corresponding 9.16-GHz ESE-detected spectrum as a function of the echo delay time,  $2\tau$ , highlighting the long-lived population in the 300–410 mT region around the hyperfine clock transition. The inset in **a** plots the normalized ESE intensity,  $I/I_0$ , at the peak in the longest-lived population at 410 mT in **b** (dashed line) as a function of delay, revealing the stretched exponential relaxation. Error bars denote the noise error, and average  $T_m$  values are indicated at different delay times.

functional theory (DFT) calculations<sup>38</sup> were performed. The converged spin-unrestricted Kohn–Sham ground states for each compound are consistent with the electronic configurations of  $[\text{Xe}]5d^1$  for **2** and  $[\text{Xe}]4f^{14}5d^1$  for **3** and **4**. The spin density for the three compounds was found to arise almost exclusively from the singly occupied molecular orbital (SOMO) in every case, with predominant  $5d_{z^2}$  character and varying degrees of  $6s$ -orbital mixing (Extended Data Fig. 4). Isotropic hyperfine coupling constants for the Ln nuclei were obtained from the computed spin density using both point and finite nuclear charge models (Table 1)<sup>39</sup>. Although the calculations systematically overestimate the coupling strength, presumably due to systematic errors in the DFT approximations and relativistic treatment<sup>40</sup>, the experimental ordering,  $2 < 3 < 4$ , is reproduced from natural population analysis of the SOMO (Extended Data Table 1)<sup>41</sup>. Two factors govern the magnitude of the hyperfine coupling in these compounds<sup>42</sup>: (1) the larger amplitude of the SOMO at the nucleus due to increasing nuclear charge and (2) an increased  $s$  character in the SOMO from La to Lu caused by greater energetic overlap between the  $5d$  and  $6s$  valence shell. The latter observation suggests that the  $s$ -orbital character,  $n(s)$ , of the SOMO is a useful descriptor of electronic structure for designing similar compounds with large hyperfine coupling.

The quadrupole coupling tensors for the Ln nuclei were also calculated in the point nuclear charge model. The results systematically underestimate the couplings compared to those obtained from EPR simulations (Table 1), but the deviations are in line with

previous benchmark DFT studies of electric field gradients<sup>43–46</sup>, showing significant variation depending on the relativistic treatment and functional used. In particular, the experimental ordering of NQI constants is reproduced ( $2 \ll 3 < 4$ ), supporting the experimental observation of a pronounced NQI in the Lu compounds. In all three cases, the principal axes of the nuclear quadrupole moments are aligned with the pseudo-three-fold symmetry axis perpendicular to the  $\text{Ln}(\text{O})_3$  and  $\text{Ln}(\text{N})_3$  planes (Extended Data Fig. 5).

## Conclusions

The main findings of this study stem from the demonstration that it is possible to control the degree of  $s$ -mixing into spin-bearing orbitals of molecular Ln(II) complexes by varying the ligands, and that this enables chemical tuning of the electron–nuclear hyperfine and quadrupole interactions, leading to a giant hyperfine clock transition frequency ( $>9$  GHz). An expected enhancement in coherence is demonstrated at this hyperfine clock transition, with a maximum  $T_m$  value exceeding  $10 \mu\text{s}$  at the relatively high temperature of 5 K, which is more than a factor of 10 longer than that of conventional EPR transitions. This work suggests routes to QIS technologies based on molecular design principles, with many parallels to approaches currently employed in more mature ion trap quantum computing architectures<sup>3</sup>.

**Note added in proof.** While this article was in press, the computational methodology used to predict hyperfine coupling constants was extended by Franzke and Yu to include additional relativistic effects<sup>47</sup>. We note that this improved method shows very good agreement with our experimental results for hyperfine coupling constants of the Lu(II) compound reported here.

## Online content

Any methods, additional references, Nature Research reporting summaries, source data, extended data, supplementary information, acknowledgements, peer review information; details of author contributions and competing interests; and statements of data and code availability are available at <https://doi.org/10.1038/s41557-022-00894-4>.

Received: 17 May 2021; Accepted: 13 January 2022;

Published online: 14 March 2022

## References

- Arute, F. et al. Quantum supremacy using a programmable superconducting processor. *Nature* **574**, 505–510 (2019).
- Devoret, M. H. & Schoelkopf, R. J. Superconducting circuits for quantum information: an outlook. *Science* **339**, 1169–1174 (2013).
- Wright, K. et al. Benchmarking an 11-qubit quantum computer. *Nat. Commun.* **10**, 5464 (2019).
- Carolan, J. et al. Universal linear optics. *Science* **349**, 711–716 (2015).
- Das Sarma, S., Freedman, M. & Nayak, C. Majorana zero modes and topological quantum computation. *Npj Quantum Inf.* **1**, 15001 (2015).
- Loss, D. & DiVincenzo, D. P. Quantum computation with quantum dots. *Phys. Rev. A* **57**, 120–126 (1998).
- Kane, B. E. A silicon-based nuclear spin quantum computer. *Nature* **393**, 133–137 (1998).
- Yang, K. et al. Coherent spin manipulation of individual atoms on a surface. *Science* **366**, 509–512 (2019).
- Thiele, S. et al. Electrically driven nuclear spin resonance in single-molecule magnets. *Science* **344**, 1135–1138 (2014).
- Gaita-Ariño, A., Luis, F., Hill, S. & Coronado, E. Molecular spins for quantum computation. *Nat. Chem.* **11**, 301–309 (2019).
- Schweiger, A. & Jeschke, G. *Principles of Pulse Electron Paramagnetic Resonance* (Oxford Univ. Press, 2001).
- Nguyen, T. N. et al. Supramolecular aggregates of single-molecule magnets: exchange-biased quantum tunneling of magnetization in a rectangular  $[\text{Mn}_3]_4$  tetramer. *Chem. Sci.* **7**, 1156–1173 (2016).
- Zadrozny, J. M., Niklas, J., Poluettov, O. G. & Freedman, D. E. Millisecond coherence time in a tunable molecular electronic spin qubit. *ACS Cent. Sci.* **1**, 488–492 (2015).

14. Shiddiq, M. et al. Enhancing coherence in molecular spin qubits via atomic clock transitions. *Nature* **531**, 348–351 (2016).
15. Zadrozny, J. M., Gallagher, A. T., Harris, T. D. & Freedman, D. E. A porous array of clock qubits. *J. Am. Chem. Soc.* **139**, 7089–7094, (2017).
16. Collett, C. A., Santini, P., Carretta, S. & Friedman, J. R. Constructing clock-transition-based two-qubit gates from dimers of molecular nanomagnets. *Phys. Rev. Res.* **2**, 032037(R) (2020).
17. Giménez-Santamarina, S., Cardona-Serra, S., Clemente-Juan, J. M., Gaita-Ariño, A. & Coronado, E. Exploiting clock transitions for the chemical design of resilient molecular spin qubits. *Chem. Sci.* **11**, 10718–10728 (2020).
18. Ghosh, S. et al. Multi-frequency EPR studies of a mononuclear holmium single-molecule magnet based on the polyoxometalate  $[\text{Ho}(\text{W}_5\text{O}_{18})_2]^{9-}$ . *Dalton Trans.* **41**, 13697–13704 (2012).
19. Miao, K. C. et al. Universal coherence protection in a solid-state spin qubit. *Science* **369**, 1493–1497 (2020).
20. Hitchcock, P. B., Lappert, M. F., Maron, L. & Protchenko, A. V. Lanthanum does form stable molecular compounds in the +2 oxidation state. *Angew. Chem. Int. Ed.* **47**, 1488–1491 (2008).
21. MacDonald, M. R., Bates, J. E., Ziller, J. W., Furche, F. & Evans, W. J. Completing the series of +2 ions for the lanthanide elements: synthesis of molecular complexes of  $\text{Pr}^{2+}$ ,  $\text{Gd}^{2+}$ ,  $\text{Tb}^{2+}$ , and  $\text{Lu}^{2+}$ . *J. Am. Chem. Soc.* **135**, 9857–9868 (2013).
22. Evans, W. J. Tutorial on the role of cyclopentadienyl ligands in the discovery of molecular complexes of the rare-earth and actinide metals in new oxidation states. *Organometallics* **35**, 3088–3100 (2016).
23. Ryan, A. J., Ziller, J. W. & Evans, W. J. The importance of the counter-cation in reductive rare-earth metal chemistry: 18-crown-6 instead of 2,2,2-cryptand allows isolation of  $[\text{Y}^{\text{II}}(\text{NR}_2)_3]^{1-}$  and ynediolate and enediolate complexes from CO reactions. *Chem. Sci.* **11**, 2006–2014 (2020).
24. Moehring, S. A. et al. Room-temperature stable Y(II) aryloxide: using steric saturation to kinetically stabilize Y(II) complexes. *Inorg. Chem.* **59**, 3207–3214 (2020).
25. Woen, D. H. & Evans, W. J. Expanding the +2 oxidation state to the rare-earth metals, uranium and thorium in molecular complexes. *Handbook on the Physics and Chemistry of the Rare Earths Including Actinides* **50**, 337–394 (2016).
26. Wolfowicz, G. et al. Atomic clock transitions in silicon-based spin qubits. *Nat. Nanotechnol.* **8**, 561–564 (2013).
27. Ariciu, M.-A. et al. Engineering electronic structure to prolong relaxation times in molecular qubits by minimising orbital angular momentum. *Nat. Commun.* **10**, 3330 (2019).
28. Anderson, D. M. et al. On the stability and bonding in bis( $\eta$ -arene)lanthanide complexes. *J. Chem. Soc. Chem. Commun.* **1989**, 53–55 (1989).
29. Knapp, C., Weiden, N. & Dinse, K.-P. EPR investigation of endofullerenes in solution. *Appl. Phys. A* **66**, 249–255 (1998).
30. Schwamm, R. J. et al. Isolation and characterization of a bismuth(II) radical. *Angew. Chem. Int. Ed.* **54**, 10630–10633 (2015).
31. Cutsail, G. E. III Applications of electron paramagnetic resonance spectroscopy to heavy main-group radicals. *Dalton Trans.* **49**, 12128–12135 (2020).
32. Smith, R. L., Wysocki, A. L. & Park, K. Electrically tuned hyperfine spectrum in neutral Tb(II)( $\text{Cp}^{\text{ipr}^2}$ )<sub>2</sub> single-molecule magnet. *Phys. Chem. Chem. Phys.* **22**, 21793–21800 (2020).
33. Stoll, S. & Schweiger, A. EasySpin, a comprehensive software package for spectral simulation and analysis in EPR. *J. Magn. Reson.* **178**, 42–55 (2006).
34. Stoll, S. & Goldfarb, D. EPR interactions—nuclear quadrupole couplings. *eMagRes* **6**, 495–510 (2017).
35. Cruikshank, P. A. S. et al. A kilowatt pulsed 94-GHz electron paramagnetic resonance spectrometer with high concentration sensitivity, high instantaneous bandwidth and low dead time. *Rev. Sci. Instrum.* **80**, 103102 (2009).
36. Schwindt, P. D. D. et al. Miniature trapped-ion frequency standard with  $^{171}\text{Yb}^+$ . In *Proc. 2015 Joint Conference of the IEEE International Frequency Control Symposium & the European Frequency and Time Forum 752–757* (IEEE, 2015); <https://doi.org/10.1109/FCS.2015.7138951>
37. Stone, N. J. Table of nuclear electric quadrupole moments. *At. Data Nucl. Data Tables* **111–112**, 1–28 (2016).
38. Peng, D., Middendorf, N., Weigend, F. & Reiher, M. An efficient implementation of two-component relativistic exact-decoupling methods for large molecules. *J. Chem. Phys.* **138**, 184105 (2013).
39. Visscher, L. & Dyall, K. G. Dirac–Fock atomic electronic structure calculations using different nuclear charge distributions. *At. Data Nucl. Data Tables* **67**, 207–224 (1997).
40. Autschbach, J. & Ziegler, P. Nuclear spin-spin coupling constants from regular approximate relativistic density functional calculations. I. Formalism and scalar relativistic results for heavy metal compounds. *J. Chem. Phys.* **113**, 936–947 (2000).
41. Reed, A. E., Weinstock, R. B. & Weinhold, F. Natural population analysis. *J. Chem. Phys.* **83**, 735–746 (1985).
42. Pykkö, P. Relativistic effects in chemistry: more common than you thought. *Ann. Rev. Phys. Chem.* **63**, 45–64 (2012).
43. Haiduke, R. L. A., da Silva, A. B. F. & Visscher, L. The nuclear electric quadrupole moment of lutetium from the molecular method. *Chem. Phys. Lett.* **445**, 95–98 (2007).
44. van Lenthe, E. & Baerends, E. Density functional calculations of nuclear quadrupole coupling constants in the zero-order regular approximation for relativistic effects. *J. Chem. Phys.* **112**, 8279–8292 (2000).
45. Schwerdtfeger, P., Pernpointner, M. & Laerdahl, J. K. The accuracy of current density functionals for the calculation of electric field gradients: a comparison with ab initio methods for HCl and CuCl. *J. Chem. Phys.* **111**, 3357–3364 (1999).
46. Srebro, M. & Autschbach, J. Does a molecule-specific density functional give an accurate electron density? The challenging case of the CuCl electric field gradient. *J. Phys. Chem. Lett.* **3**, 576–581 (2012).
47. Franzke, Y. J. & Yu, J. M. Hyperfine coupling constants in local exact two-component theory. *J. Chem. Theory Comput.* **18**, 323–343 (2022).

**Publisher's note** Springer Nature remains neutral with regard to jurisdictional claims in published maps and institutional affiliations.

© The Author(s), under exclusive licence to Springer Nature Limited 2022

## Methods

**Synthesis.** The La(II) and Lu(II) compounds examined in this study were obtained by potassium reduction of Ln(III) compounds in the presence of 2,2,2-cryptand (crypt), as shown in Extended Data Fig. 6 for Lu with the 2,6-Ad<sub>3</sub>-4'-Bu-C<sub>6</sub>H<sub>4</sub>O (OAr<sup>+</sup>) ligand. All reduction reactions gave dark solutions characteristic of 4f<sup>n</sup>5d<sup>1</sup>Ln(II) ions<sup>22</sup>. Both Lu(OAr<sup>+</sup>)<sub>3</sub> (Supplementary Fig. 1) and [K(crypt)] [Lu(OAr<sup>+</sup>)<sub>3</sub>] (4) (Fig. 1 and Supplementary Fig. 2) were crystallographically characterized (Supplementary Tables 1 and 2). Neither the dark solution, 2, formed by reducing La(OAr<sup>+</sup>)<sub>3</sub>, nor the dark solution, 3, formed by reducing Lu(NR<sub>2</sub>)<sub>3</sub>, provided X-ray-quality crystals, although the analogous [K(18-c-6)] [Y(NR<sub>2</sub>)<sub>3</sub>]<sup>23</sup> and tris(aryloxy) [K(crypt)] [Y(OAr<sup>+</sup>)<sub>3</sub>]<sup>24</sup> have been crystallographically characterized. See Supplementary Section 2 for further synthetic details.

**Sample handling.** Owing to the reactive nature of the studied compounds, all manipulations and loading of samples into EPR tubes were performed in a glovebox at UC Irvine, as described in detail in Supplementary Section 2. Samples of 2–4 were diluted to 1, 5, 10 and 20 mM concentrations in tetrahydrofuran solvent to minimize electron spin–spin dipolar interactions. Only the 10 mM solution was studied by EPR. The solution samples were immediately frozen in EPR tubes and shipped overnight to the US National High Magnetic Field Laboratory (NHMFL) in a dry cryogenic shipper (at –196 °C), where they were transferred into storage under liquid nitrogen. Both of the spectrometers employed in this study have been designed for rapid cold loading of frozen samples<sup>35</sup>. These steps prevented degradation of the samples before study, as borne out by the experimental results, which confirm Ln(II) species in every case.

**EPR measurements.** High-field (W-band) spectra were recorded at 94.0 GHz using the high-power pulsed EPR spectrometer, HiPER<sup>35</sup>, at the NHMFL. Developed at the University of St Andrews, HiPER employs a quasi-optical design that allows for inductive mode detection, whereby the returning echo signal is isolated from the high-power excitation pulses by detecting in the orthogonal polarization. These factors (high power and inductive mode) and the possibility to study relatively large sample volumes using non-resonant sample holders<sup>38</sup> provide excellent sensitivity for low-concentration samples. We used fluorinated ethylene propylene tubes with an inner diameter (ID) of 2 mm, allowing for a 60-μl sample volume in all cases. Field-swept ESE detected spectra for all three compounds were obtained using a standard Hahn-echo pulse sequence,  $\pi/2-\tau-\pi-\tau$ -echo, where the duration of the  $\pi/2$  pulse was 100 ns and the delay  $\tau = 400$  ns, and the integration window spanned the full echo signal. Although the spectrometer can deliver shorter pulses, the microwave power was reduced and the 100-ns  $\pi/2$  pulse length was chosen to avoid spectral broadening due to the finite excitation bandwidth ( $1/T_{\text{exc}} \approx 10$  MHz). Final adjustments to the power were made to ensure optimum rotation ( $\pi/2, \pi$ ) of the magnetization. The magnetic field was swept from 2.8 to 4.2 T with a step size of 1 mT, and the signal was recorded as an average of 1,000 shots at each step. The magnetic field was generated by a sweepable high-resolution (20 ppm over 1-cm DSV) superconducting magnet, while the temperature was controlled using a continuous-helium-flow cryostat (both Oxford Instruments).

X-band ESE-detected spectra and relaxation time ( $T_m$  and  $T_1$ ) measurements were performed in the frequency range from 9.11 to 9.5 GHz using a commercial spectrometer (Bruker E680) equipped with a dielectric resonator (ER4118X-MD5). The temperature was regulated at 5 K during all measurements using a CF1200 helium-flow cryostat (Oxford Instruments). Standard 4-mm-outer-diameter (3-mm ID) quartz EPR tubes were filled to a height of ~1.5 cm (that is, a volume of ~100 μl). All Hahn-echo measurements were performed using a 48-ns  $\pi/2$  pulse length. The microwave power was optimized for the strongest ESE-detected peak observed in the 750-mT range (Fig. 4 and Extended Data Fig. 2), requiring attenuation of the microwave power in the –3 to –5 dB range. The field-swept ESE-detected spectra in Fig. 4 were recorded using an inter-pulse delay time of  $\tau = 300$  ns, and the data in Fig. 5b employed variable delays.

The X-band resonator is configured to excite perpendicular-mode transitions when optimally tuned to its 9.80-GHz centre frequency. However, it was maximally over-coupled for these investigations to provide enough bandwidth for measurements down to the lowest frequency of 9.11 GHz achievable with the travelling-wave tube amplifier associated with the spectrometer. As noted in a previous study<sup>14</sup>, the resonator is known to also excite parallel-mode transitions. Indeed, a scan of the  $B_1$  field in the resonator reveals a local maximum at 9.2 GHz that is evident even in the spectrometer operating manual. When over-coupled, the convolution of the resonator, source/amplifier and beam propagation system responses yields an asymmetric profile, peaking at a  $B_1$  field (@ 0-dB attenuation) of ~9.0 G at 9.80 GHz, with a slow drop-off to ~3.5 G at 9.11 GHz on the low-frequency side, and a local maximum of 6.0 G at 9.20 GHz, suggesting possible contamination of the fundamental resonance with a mode that possesses a  $\mathbf{B}_1 \parallel \mathbf{B}_0$  component. The presence of perpendicular-mode resonances in the spectra provides a much better opportunity to calibrate the parallel-mode contamination in the present investigation. To this end, the best simulations in Fig. 4c were generated by adding a parallel-mode component,  $I_p$ , to the perpendicular-mode intensity,  $I_x$  (Extended Data Fig. 2), with a frequency-dependent amplitude  $a_p(f)$  for the former, that is, a summed intensity,  $I(f) = I_x + a_p(f)I_p$ , where  $a_p(f)$  is a Lorentzian function with a centre frequency of 9.2 GHz, FWHM of 0.1 GHz and peak

value of 1.2. As can be seen in Fig. 4, this produces excellent simulations of the experimental results. It implies that the spectrum is mostly perpendicular-mode at the highest frequency of 9.5 GHz, hence the almost vanishing 7 → 9 signal at 500 mT. Meanwhile, there is ~30% contamination at the lowest frequency of 9.11 GHz, and 120% contamination at the 9.2-GHz maximum. The fact that a Lorentzian admixture accounts for the results so well is fully consistent with mode contamination. Finally, we note that the colour map in Fig. 4a employed a 50:50 mixture of  $I_x$  and  $I_p$ , primarily to emphasize the frequency dependence of the 7 → 9 transition.

**Spin Hamiltonian and nuclear quadrupole interaction.** The effective spin Hamiltonian describing a lone unpaired  $S = 1/2$  electron coupled to a single  $I = 7/2$  nuclear spin is given by equation (1), where  $\mu_B$  ( $\mu_N$ ) is the Bohr (nuclear) magneton and  $g_n$  the nuclear  $g$ -factor, while  $\hat{S}$  and  $\hat{I}$  represent the electron and nuclear spin operators, respectively. The hyperfine coupling tensor,  $\hat{A}$ , is diagonal, with components  $A_i$  ( $i = x, y, z$ ). Meanwhile, our analysis requires inclusion of an NQI specified by the traceless diagonal matrix  $\hat{Q}$  (equation (2), in frequency units)<sup>34</sup>. In the principal axes system of the diagonal electric field gradient (EFG) tensor,  $\hat{V}$ , the NQI tensor can be written as

$$\hat{Q} = \begin{pmatrix} Q_{xx} & 0 & 0 \\ 0 & Q_{yy} & 0 \\ 0 & 0 & Q_{zz} \end{pmatrix} = \frac{eQV_{zz}/h}{4I(2I-1)} \begin{pmatrix} -(1-\eta) & 0 & 0 \\ 0 & -(1+\eta) & 0 \\ 0 & 0 & 2 \end{pmatrix}, \quad (2)$$

where  $e$  is the elementary charge,  $Q$  is the nuclear quadrupole moment,  $V_{zz}$  is the principal component of the diagonal EFG tensor and  $\eta$  is a dimensionless asymmetry parameter. All spectral simulations have been generated via exact diagonalization of equation (1) using the program EasySpin<sup>49</sup>. The parameters obtained from the best simulations are given in Table 1. An axial NQI was assumed ( $\eta = 0$ ), primarily because of the approximate trigonal symmetry of the studied compounds, but also because there were no noticeable improvements in the simulations upon including a finite  $\eta$  parameter. For further details, see Supplementary Sections 3 and 5.

**Computational details.** All-electron DFT calculations were performed using the TPSS<sup>50</sup> functional for each compound and the self-consistent field (SCF) procedure was converged to  $10^{-7}$  Hartree ( $E_h$ ). x2c-TZVPPall-s basis sets were used for the Ln centres, and x2c-SVPall basis sets were used for each respective ligand atom<sup>51</sup>. Relativistic corrections were included using the all-electron variational x2c method, both with and without including spin-orbital coupling effects<sup>52</sup>. The finite nucleus model<sup>39</sup> and local approximation<sup>33</sup> were also used in the relativistic treatment. All calculations were performed using the TURBOMOLE V7.5 quantum chemistry software<sup>54</sup>. See Supplementary Section 5 for further details.

## Data availability

All data that support the findings of this study are available via the Open Science Framework (OSF, <https://osf.io/jr3dq/>) with the identifier <https://doi.org/10.17605/OSF.IO/JR3DQ5>. These data include the EPR results presented in the main paper, the optimized coordinate files from the computational studies, as well as the X-ray, <sup>1</sup>H/<sup>13</sup>C NMR, infrared and UV–vis spectra in the Supplementary Information. The available crystallographic data have also been deposited at the Cambridge Crystallographic Data Centre under the following deposition numbers: [K(crypt)]<sup>+</sup>[Lu<sup>III</sup>(OAr<sup>+</sup>)<sub>3</sub>]<sup>-</sup>, compound 4, CCDC 2074946 and Lu<sup>III</sup>(OAr<sup>+</sup>)<sub>3</sub>, CCDC 2074947. Copies of the data can be obtained free of charge via <https://www.ccdc.cam.ac.uk/structures/>. Source data are provided with this paper.

## Code availability

All computer codes employed in this study are available in the cited references.

## References

- Song, L. et al. Towards increased concentration sensitivity for continuous wave EPR investigations of spin-labeled biological macromolecules at high fields. *J. Magn. Res.* **265**, 188–196 (2016).
- EasySpin; <https://easyspin.org>
- Staroverov, V. N., Scuseria, G. E., Tao, J. & Perdew, J. P. Comparative assessment of a new nonempirical density functional: molecules and hydrogen-bonded complexes. *J. Chem. Phys.* **119**, 12129–12137 (2003).
- Franzke, Y. J., Treß, R., Pazdera, T. M. & Weigend, F. Error-consistent segmented contracted all-electron relativistic basis sets of double- and triple-zeta quality for NMR shielding constants. *Phys. Chem. Chem. Phys.* **21**, 16658–16664 (2019).
- Franzke, Y. J., Middendorf, N. N. & Weigend, F. Efficient implementation of one- and two-component analytical energy gradients in exact two-component theory. *J. Chem. Phys.* **148**, 104110 (2018).
- Peng, D. & Reiher, M. J. Local relativistic exact decoupling. *Chem. Phys.* **136**, 244108 (2012).

54. Balasubramani, S. G. et al. TURBOMOLE: modular program suite for ab initio quantum-chemical and condensed-matter simulations. *J. Chem. Phys.* **152**, 184107 (2020).
55. Hill, S. et al. 9.2-GHz clock transition in a Lu(II) molecular spin qubit arising from a 3,467-MHz hyperfine interaction (OSF, 2021); <https://doi.org/10.17605/OSF.IO/JR3DQ>

### Acknowledgements

We thank the US National Science Foundation (NSF; CHE-1855328 to W.J.E. and CHE-1800431 and CHE-2102568 to F.F.) and the Department of Energy (DE-SC0020260 to S.H.) for support of this research. Work performed at the NHMFL is supported by the NSF (DMR-1644779) and by the State of Florida. J.M.Y. acknowledges support of the NSF Graduate Research Fellowship Program (DGE-1839285). We also thank the Eddleman Quantum Institute for promoting this collaborative project.

### Author contributions

W.J.E., F.F. and S.H. conceived the research. J.R.K.W. and S.A.M. prepared the samples, S.H. and K.K. designed the experiments. K.K. performed the measurements. K.K. and

S.H. analysed the EPR results, J.W.Z. performed the X-ray structural analysis. J.M.Y. and F.F. formulated and executed the computational analysis. All authors contributed to the writing of the manuscript.

### Competing interests

The authors declare no competing interests.

### Additional information

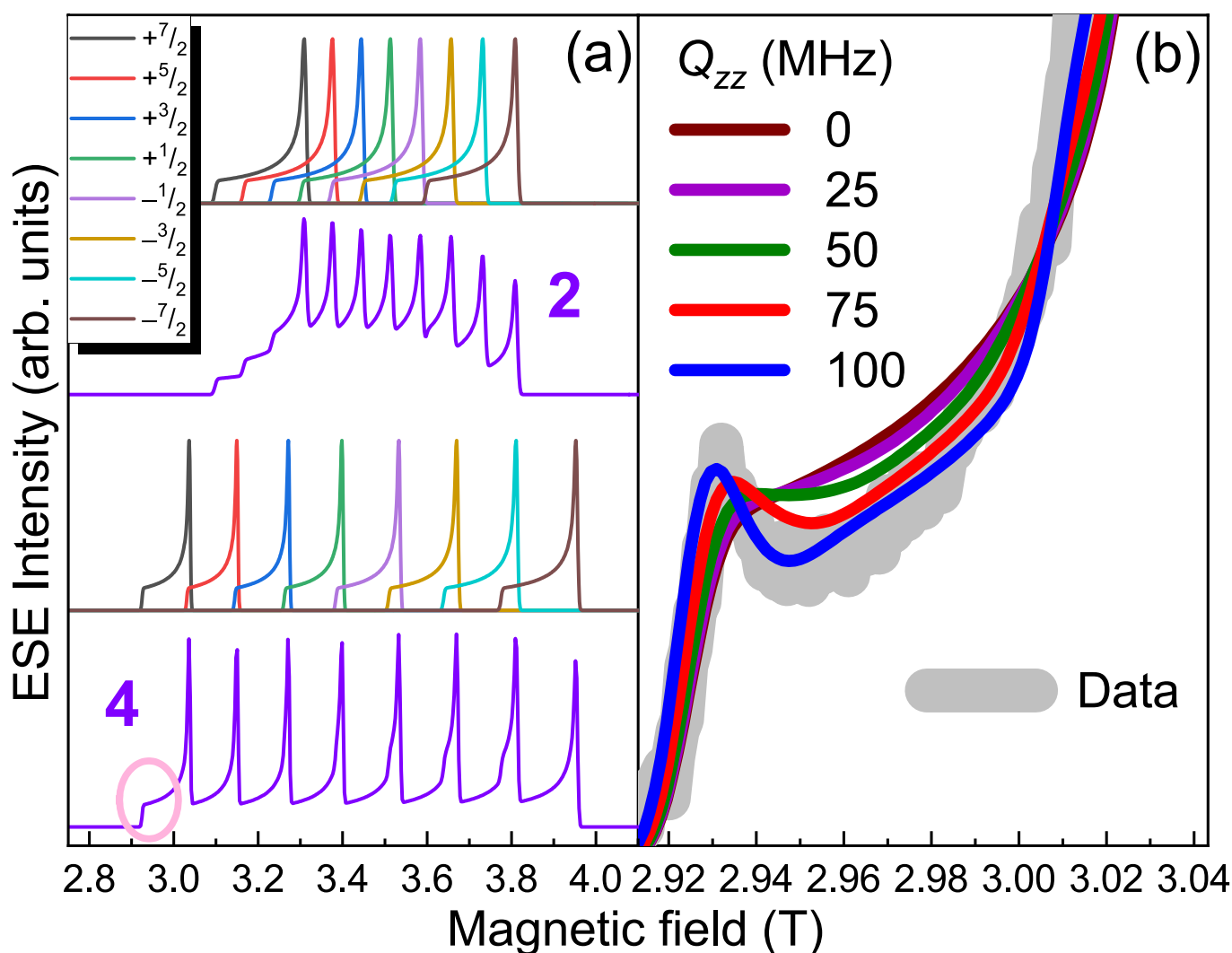
**Extended data** is available for this paper at <https://doi.org/10.1038/s41557-022-00894-4>.

**Supplementary information** The online version contains supplementary material available at <https://doi.org/10.1038/s41557-022-00894-4>.

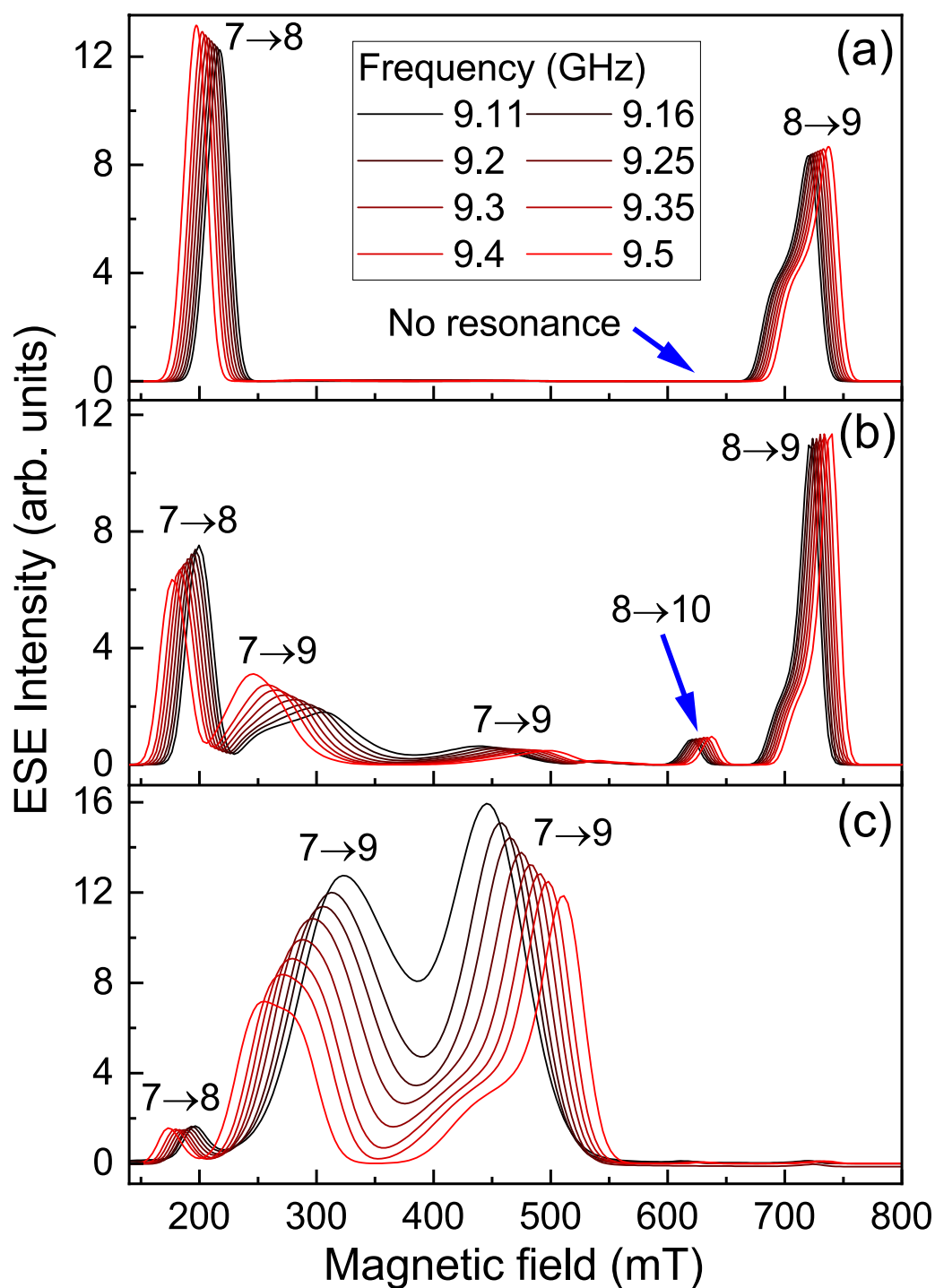
**Correspondence and requests for materials** should be addressed to Filipp Furche, William J. Evans or Stephen Hill.

**Peer review information** *Nature Chemistry* thanks the anonymous reviewers for their contribution to the peer review of this work.

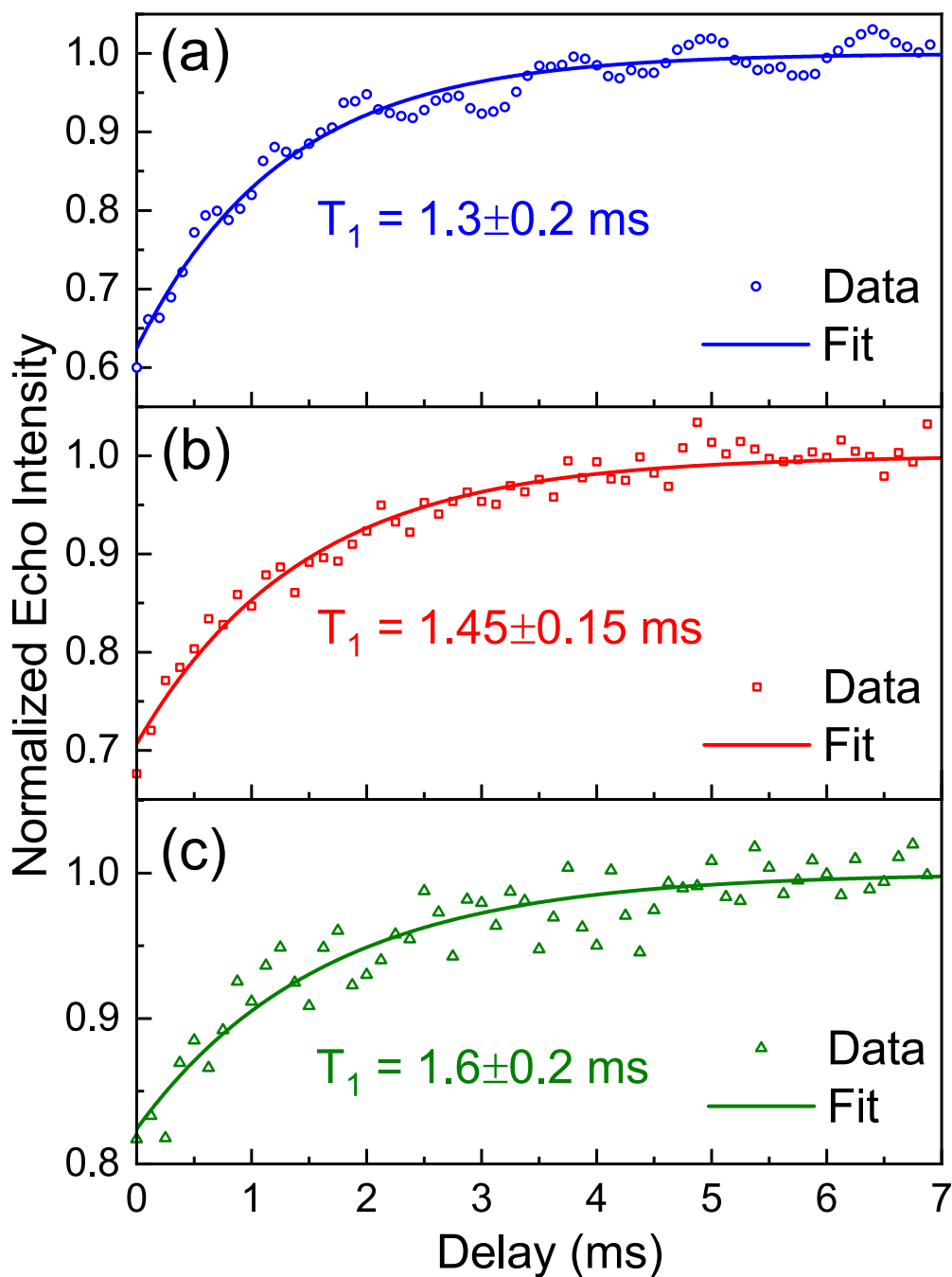
**Reprints and permissions information** is available at [www.nature.com/reprints](http://www.nature.com/reprints).



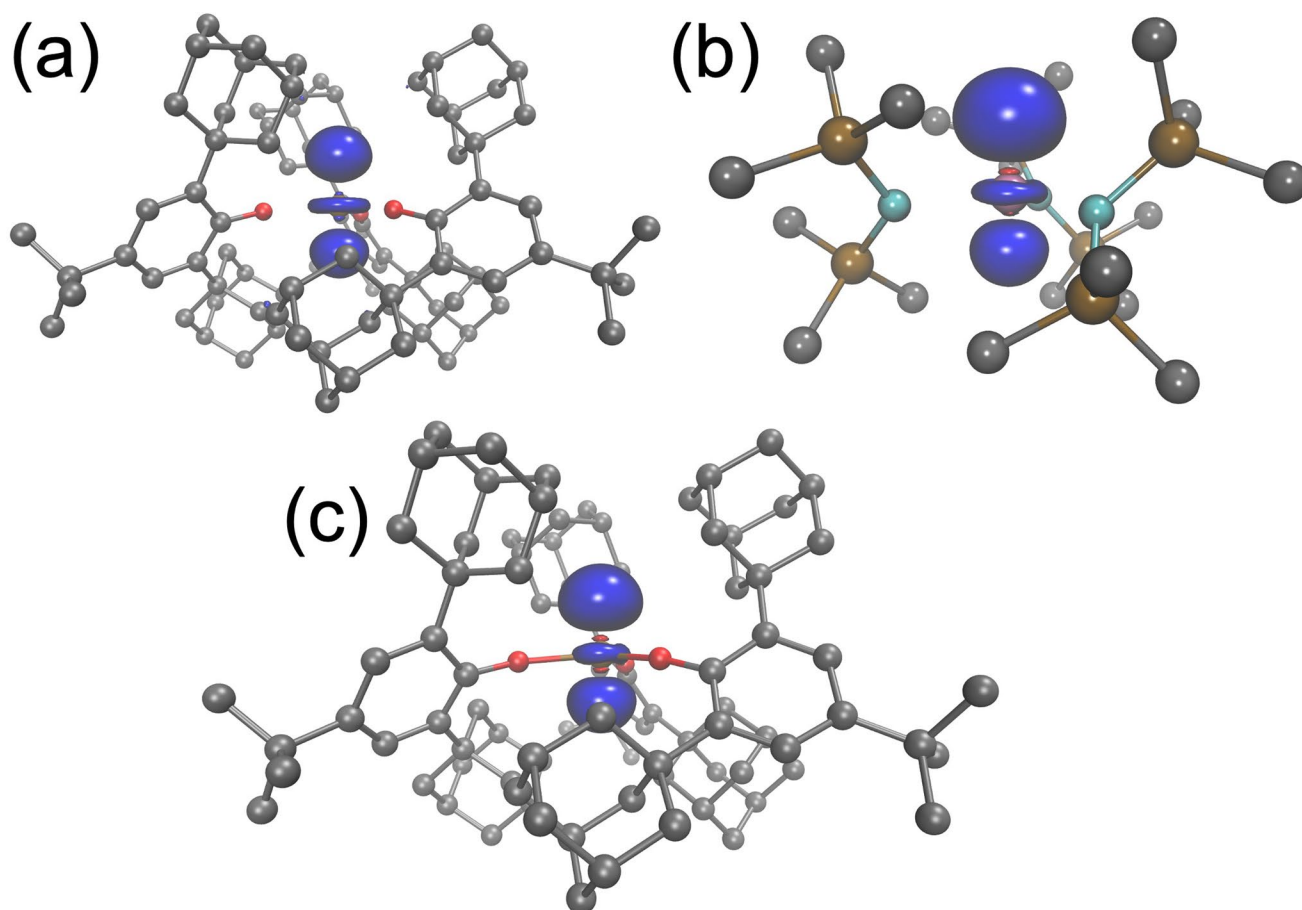
**Extended Data Fig. 1 | EPR spectral lineshapes.** (a) Qualitative simulations of the ESE intensity patterns observed for compounds **2** and **4**. The full spectra (in purple) were generated by summing individual hyperfine components – the eight colored curves above each summed spectrum, labeled according to the associated nuclear projection,  $m$ . The asymmetric lineshapes of the individual components are dictated by the  $\vec{g}$ -tensor anisotropy and the spacing by the hyperfine and nuclear quadrupole interactions. These simulations capture the main features observed in the experimental spectra, particularly the staircase increase in intensity on the low-field side of the spectrum for **2**. The pink oval highlights the region of the spectrum shown in (b). (b) Zoomed region of the experimental spectrum of **4**, from Fig. 3c, showing the feature that is very sensitive to the NQI. Superimposed are simulations for different values of  $Q_{zz}$ , from which the optimum value of  $100 \pm 20$  MHz is deduced (Table 1). We note that the qualitative simulations in (a) do not explicitly take into account the NQI, whereas the exact simulations in (b) do; for further details, see Supplementary Information Section 3.



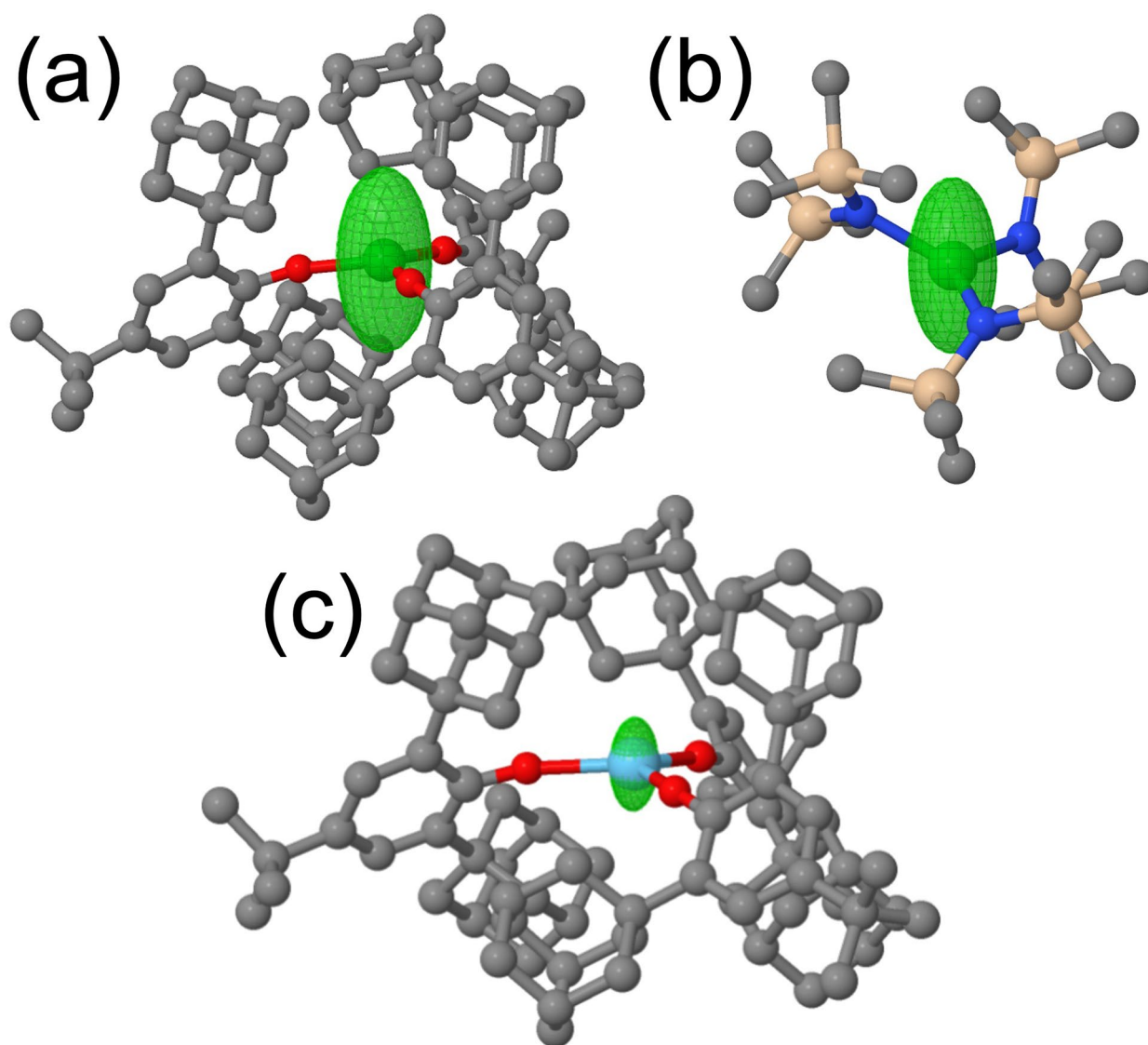
**Extended Data Fig. 2 | Parallel and perpendicular mode X-band simulations.** (a) Perpendicular mode simulations using parameters from Table 1, but with  $Q_{zz}=0$ . The important thing to note is the absence of the weakly allowed  $8 \rightarrow 10$  resonance that is clearly seen in the experimental spectra (Fig. 4). (b) The  $8 \rightarrow 10$  resonance appears upon inclusion of the NQI in the perpendicular mode simulations, with  $Q_{zz}=100$  MHz correctly reproducing the relative intensities of the  $8 \rightarrow 9$  and  $8 \rightarrow 10$  resonances, which are only seen in the perpendicular mode simulations. (c) Parallel mode simulations with full parameterization in Table 1. A frequency dependent mixture of perpendicular and parallel simulations is needed for the simulations in Fig. 4 (see Methods). Although the units are arbitrary, the three panels are presented in the same absolute scale, that is, the simulations have not been rescaled.



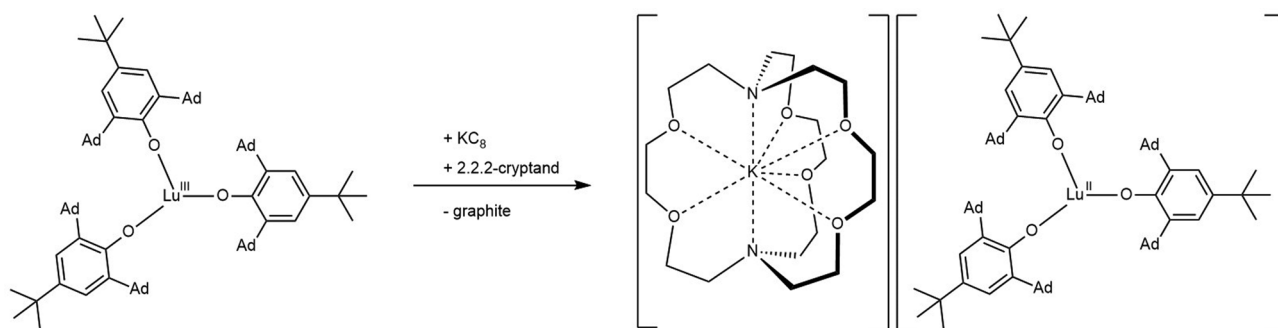
**Extended Data Fig. 3 | Spin-lattice ( $T_1$ ) relaxation measurements for 4.** ESE saturation recovery measurements at 310 (a), 410 (b) and 720 mT (c); the frequency was 9.16 GHz and the temperature 5 K.  $T_1$  times deduced from exponential fits are displayed in each panel; the uncertainties correspond to the standard errors. See Supplementary Information Section 4 for further details.



**Extended Data Fig. 4 | Spin density calculations.** Contours of the spin density (blue) computed with DFT for compounds **2** (a), **3** (b), and **4** (c), plotted at a contour value of 0.005. Hydrogen atoms have been omitted. Color codes: Grey = C, Red = O, Brown = Si, Teal = N, Pink = Ln.



**Extended Data Fig. 5 | Ellipsoid plots of the nuclear quadrupole moment tensor.** Visualization of the quadrupole tensors arising from the Ln nucleus computed with DFT for compounds **4** (a), **3** (b), and **2** (c). Because  $\eta$  is small, the ellipsoids are effectively spheroidal in all three cases. Scaling factors,  $s$ , of  $5.5 \times 10^3$ ,  $5.5 \times 10^3$ , and  $1.65 \times 10^4$  were applied in (a), (b), and (c), respectively; see Supplementary Information Section 5 for further details. Hydrogen atoms were omitted for clarity. Color codes: Grey=C, Red=O, Tan=Si, Blue=N, Teal=Ln.



**Extended Data Fig. 6 | Synthesis of  $[K(\text{crypt})][\text{Lu}(\text{OAr}^*)_3]$ , **4**.** Potassium reduction of  $\text{Lu}(\text{OAr}^*)_3$  in the presence of 2.2.2-cryptand yields  $[K(\text{crypt})][\text{Lu}(\text{OAr}^*)_3]$ .

**Extended Data Table 1** | Natural population analysis. Natural atomic populations [n(s), etc.] of the SOMO arising from Ln = La or Lu for compounds 2–4 (see Supplementary Information Section 5 for further details)

Compound	n(s)	n(p)	n(d)	n(f)
[Lu(OAr <sup>+</sup> ) <sub>3</sub> ] <sup>-</sup> <b>4</b>	0.346	0.039	0.483	0.003
[Lu(N <sup>+</sup> ) <sub>3</sub> ] <sup>-</sup> <b>3</b>	0.276	0.074	0.531	0.002
[La(OAr <sup>+</sup> ) <sub>3</sub> ] <sup>-</sup> <b>2</b>	0.265	0.018	0.544	0.002